Hindawi
Advances in Civil Engineering
Volume 2018, Article ID 4720564, 9 pages
https://doi.org/10.1155/2018/4720564

Research Article

Effect of Low-Stress Fatigue on the Off-Crack-Plane Fracture Energy in Engineered Cementitious Composites

Longlong Liu,[1] **Shuling Gao**,[2] **Jianda Xin**,[3] **and Dahai Huang**[1]

[1]*School of Transportation Science and Engineering, Beihang University, Beijing 100191, China*
[2]*School of Civil and Transportation Engineering, Hebei University of Technology, Tianjin 300401, China*
[3]*Department of Structures and Materials, China Institute of Water Resources and Hydropower Research, Beijing 100038, China*

Correspondence should be addressed to Dahai Huang; 59703751@qq.com

Received 27 August 2017; Revised 16 November 2017; Accepted 21 November 2017; Published 4 March 2018

Academic Editor: Peng Zhang

This paper presented an experimental study on the flexural properties of engineered cementitious composites (ECCs). The bending fatigue damage, residual deformation, and damage characteristics were investigated after a certain number of low stress levels in fatigue load. The composite fracture energy and fiber-bridging fracture energy were calculated by the J integral. It is observed that the number of cracks increased with the increment of stress levels, and most of the cracks were formed during the earlier stage of the dynamic test. The deformation capability decreased with the increment of stress levels while the reduction of the ultimate load was minor after the dynamic load. Furthermore, the strain-hardening phenomenon of the specimen enhanced initially and then weakened with the increment of stress levels. The residual equivalent yield strength became smaller with the increase of stress levels. Meanwhile, the trend was mild at low stress levels and then became steep at high stress levels.

1. Introduction

The engineered cementitious composites (ECCs), as a common composite, have been used for many important parts of the structure. There are lots of methods to model the fracture failure behavior in the ECC since its service life time and function depend on the stress levels to a large extent. By virtue of the three-point bending tests, Elices et al. [1] calculated the fracture energy (G_F), which is used as a parameter to present the performance of many composite materials. Li and Hashida [2] obtained the total fracture energy which is 34 kJ/m^2 of the ECC with 4% of the fiber volume fraction by making a finite element analysis about the fracture through the J integral. Zhang et al. [3, 4] established the bending model and found the relationship of the flexural resistance and the specimen thickness. Zhang and Stang [5] investigated the relationship of the crack length and fatigue cycles in the ECC fatigue fracture test. The strain and crack width brought about by the increase of the fatigue cycles cause the interfacial degradation in fiber composite materials, but the crack width is no more 100 μm before the main crack localizes. Thus, the effect of crack width on fracture properties of specimens is ignored in this paper [1, 6–9].

The fatigue test under the high stress level is done, and the relationship between the stress level and the fatigue life has been proven to be linear in logarithm [8–10]. Through the linear logarithmic equation, we can estimate the fatigue life under low stress levels, but the fatigue test under low stress levels has been seldom attempted [10]. The common ECC specimens are normally difficult to achieve fatigue damage when they are under low stress levels, let alone the ECC specimens with the characteristics of metal fatigue.

Owing to the difficulty of achieving fatigue damage, the crack length, crack mouth opening displacement (CMOD), and ultimate load were measured during static damage after the certain cycles of fatigue under the stress levels of 0.23, 0.26, 0.34, 0.55, 0.59, and 0.65. In this paper, a series of experiments regarding the three-point bending fatigue fracture under low stress were conducted to investigate the residual fracture energy and the residual equivalent yield strength.

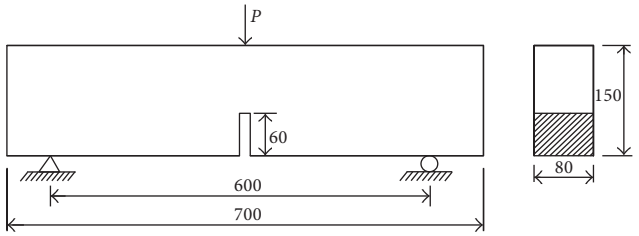

Figure 1: Three-point bending specimen's geometry and dimensions (mm).

Table 1: Properties of the PVA fiber.

Length (mm)	Diameter (μm)	Nominal strength (MPa)	Fiber elongation (%)	Young's modulus (GPa)	Density (kg/m^3)
12	18	1600	7	42	1300

2. Determination of Fracture Parameters of the Three-Point Bending Test of ECC

2.1. Specimen Dimensions and Materials. The three-point bending test specimens were cast in wood former with dimensions of 700 mm × 150 mm × 80 mm (Figure 1). The prefabricated crack was embedded with a 3 mm thick steel plate, and the height of the crack was 60 mm [11]. After the casting was completed, the specimens were remolded until they had been sealed for curing for 24 hours. Then, they were maintained for 100 days at the laboratory temperature (at about 20°C).

Each specimen had the same mix proportion. The mix proportion was as follows: cement : fly ash : sand : water = 1 : 3.5 : 2.3 : 1.28. The cement adopted was P.O42.5 silicate cement. As quartz sand, it was hard and good artificial sand, in which the fineness modulus was less than 2.65 and the percent of mud was not more than 1.5%. With the increment of fiber volume fraction, the compressive strength, the tensile strength, and the fracture toughness of the ECC increase. In contrast, its mechanical performance enhances slightly when the fiber volume fraction increases to 2% [12–15]. Under this situation, the ECC with 2% of the fiber volume fraction shows good performance. Hence, the same fiber volume fraction was applied in the test. Table 1 shows the corresponding properties of the polyvinyl alcohol (PVA) fiber. Grade I composite fly ash was used. The compressive strength of the specimen was 36.6 MPa at 28 days [16].

2.2. Test Equipment and Test Procedure. The whole loading procedure was completed by means of the servohydraulic system made in Beijing Foli System Company, China. A dynamic sampling system produced by Donghua Testing Technology Co. Ltd. was adopted to collect data.

2.2.1. Static Test. Figure 1 illustrates the setup for the static test, where a vertical, linear load was applied onto the middle of the beam's top surface, using a compression test device.

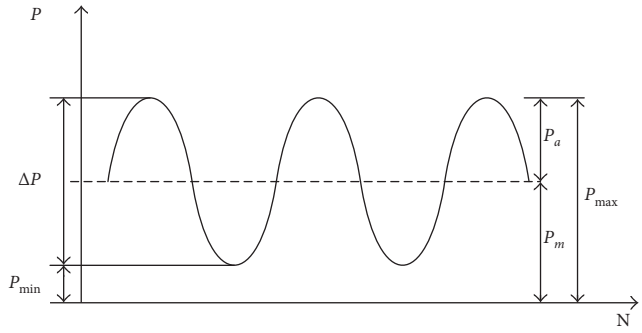

Figure 2: Relation among load parameters for the fatigue test.

With the specimens resting on two line supports with a span length of 600 mm, the load (P) was continuously recorded by the sampling system, and the middle displacement was measured by the displacement gauge. The opening of the crack mouth opening displacement (CMOD) was measured by the clip gauge. The loading method was controlled by the middle displacement with the loading rate of 0.05 mm/min [3–5, 17].

2.2.2. Dynamic Test. The dynamic tests were conducted by the load control mode with the frequency of 1 Hz. The load shape was a sine wave shown in Figure 2 [2, 12, 18, 19]. In the test process, the maximum load (P_{max}) based on the ultimate load of specimens in the static test, the average load (P_m), the load range, the load amplitude (P_a), and the minimum load (P_{min}) can be calculated by (1)–(4). The length and width of the crack with corresponding time and fatigue cycles were recorded by observation every ten minutes [8, 9, 13, 20, 21].

$$P_m = \frac{P_{max} + P_{min}}{2}, \tag{1}$$

$$P_a = \frac{P_{max} - P_{min}}{2}, \tag{2}$$

$$\Delta P = 2P_a, \tag{3}$$

$$R = \frac{P_{min}}{P_{max}}, \tag{4}$$

where P_{max}, P_{min}, P_m, P_a, and ΔP are shown in Figure 2. R is the characteristic value of the load.

2.2.3. Calculation Methods. The J integral value for the three-point bending specimens is calculated by the curve of load-displacement according to the provisions of the ASTM E-24 [22]. J represents the fracture energy dissipation during the cracking process. The fracture energy, the J integral value [23], is then calculated according to the following equation:

$$J = \frac{2A}{t(h - a_0)}, \tag{5}$$

where t and h represent the specimen width and height, respectively. The initial crack depth is denoted by a_0, while A denotes the area of the curve of load-displacement [24–27]. As the midspan deflection has a good linear relationship with the CMOD for the tested specimens, in this paper, A is calculated by the P-CMOD curves [13].

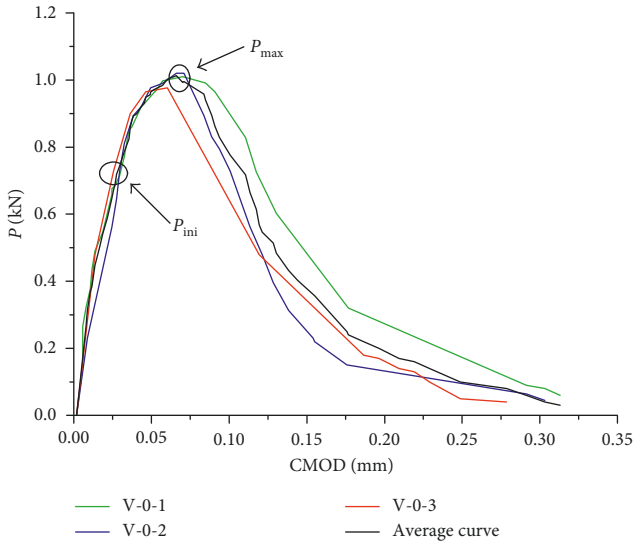

Figure 3: Matrix of *P*-CMOD curves under static load.

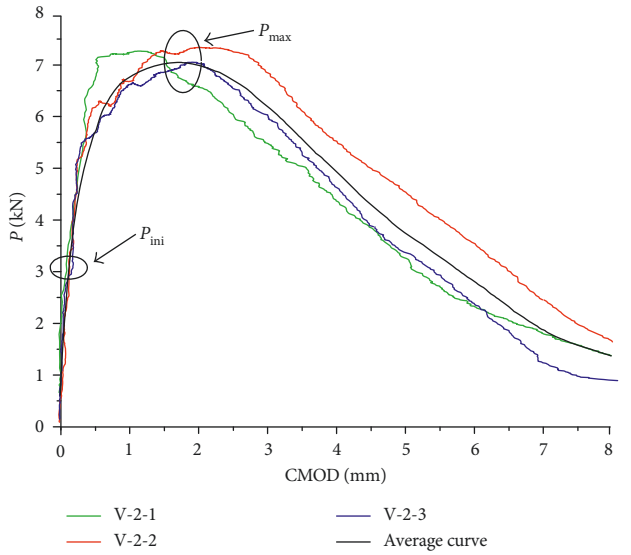

Figure 4: ECC of *P*-CMOD curves under static load.

Following the double-*K* fracture criterion of concrete [28], Liu et al. [13] proposed the J_{IC}, the starting point of the ductile stage, and the J_{IF}, the starting point of the failure stage. The first crack appeared when $J > J_{IC}$, the localized failure crack developed when $J > J_{IF}$, and the material was in a safe state when $J \leq J_{IF}$ [13]. So, the threshold of fracture and failure can be applied to estimate the fracture toughness of the ECC material. Furthermore, J_C, the total fracture energy, which includes all the loading processes can also be calculated by (5).

3. Results and Discussions

3.1. Static Test Results

3.1.1. P-CMOD Curves. The *P*-CMOD curves of static load specimens, the average curves for the ECC and matrix acquired by calculating the mean force at fixed CMOD values, are displayed in Figures 3 and 4. The fracture surface magnified 200 times is shown in Figure 5. A summary of the initial cracking load (P_{ini}), peak load (P_{max}), and the corresponding CMOD values is also provided in Table 2. It can be seen that the initial cracking load increased with adding PVA fibers in the specimens [14]. The fibers increased the initial cracking load and delayed the cracking time compared to the matrix. The corresponding CMOD values of the initial cracking load of the ECC increased much greater than those of the matrix, which demonstrated that the load was transmitted across the PVA fibers as well [29].

3.1.2. Fracture Parameters. Table 2 shows the results of the fracture parameters calculated by (5). P_{ini} is measured by strain gauges pasted on the surface of specimens, that is, the cracking load of the ECC [13]. P_{max} is the maximum load during the loading process; meanwhile, the $CMOD_C$ value happens. It is clear that the beams made from the matrix had small cracking resistance since they generated the lowest values for J_{IC} and J_{IF} (Table 2) [13]. Figure 5(a) shows that some fibers were pulled out or cut from mortar, meaning that the fibers were pulled out when the specimens could absorb energy. According to the frictional resistance between the fibers and mortar, some other fibers (Figure 5(b)), however, are ruptured when they consume more energy [6, 30, 31]. The average initial cracking energy of the ECC is 3 times that of the matrix. The average failure fracture energy of the ECC is 7.77 kJ/m^2, which is approximately 740 times that of the matrix. The ultimate load can be determined as 7 kN according to the average value of ultimate load of three specimens [16].

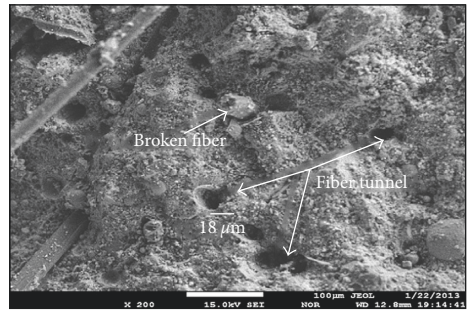

(a)

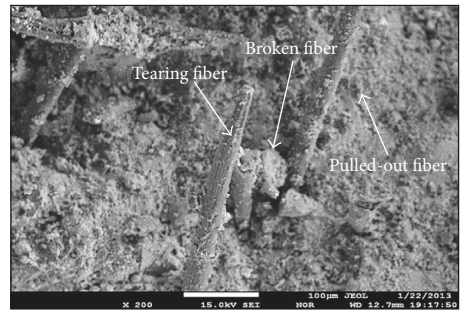

(b)

Figure 5: Typical cracking surface under the optical investigation of ECC specimen (V-2-1).

Table 2: Fracture parameters from three-point bending beams.

Specimen number	a_0 (mm)	P_{ini} (kN)	P_{max} (kN)	$CMOD_C$ (mm)	J_{IC} (kJ/m^2)	J_{IF} (kJ/m^2)
V-0-1	60	0.74	0.902	0.049	0.011	0.012
V-0-2	60	0. 8	0.962	0.053	0.0081	0.0085
V-0-3	60	0.82	1.052	0.051	0.008	0.011
Average	—	0.79	0.972	0.051	0.009	0.0105
V-2-1	60	2.75	7.02	2.12	0.035	8.1
V-2-2	60	2.55	6.9	2.33	0.032	7.9
V-2-3	60	3	7.1	1.91	0.038	7.3
Average	—	2.77	7	2.12	0.035	7.77

Note. V-0 and V-2 represent the fiber volume fraction of 0 and 2% in the ECC, respectively.

Table 3: Fatigue loads and corresponding stress levels.

Specimen number	Average load, P_m (kN)	Amplitude, P_a (kN)	Maximum load, P_{max} (kN)	Minimum load, P_{min} (kN)	Stress level, S	Load eigen value, R	Fatigue cycles, N
TPB-1	0.89	0.75	1.7	0.113	0.23	0.081	10,000
TPB-2	0.92	0.75	1.7	0.132	0.26	0.08	10,000
TPB-3	1.335	1.04	2.372	0.298	0.34	0.11	10,000
TPB-4	2.418	1.7	3.881	0.414	0.55	0.107	10,000
TPB-5	2.487	1.7	4.107	0.867	0.59	0.21	10,000
TPB-6	3	1.5	4.55	1.5	0.65	0.33	10,000

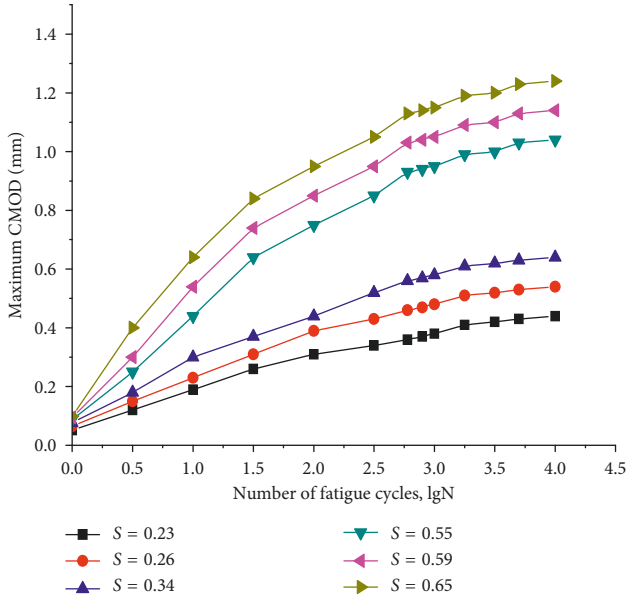

Figure 6: Evolution of CMOD during the dynamic test.

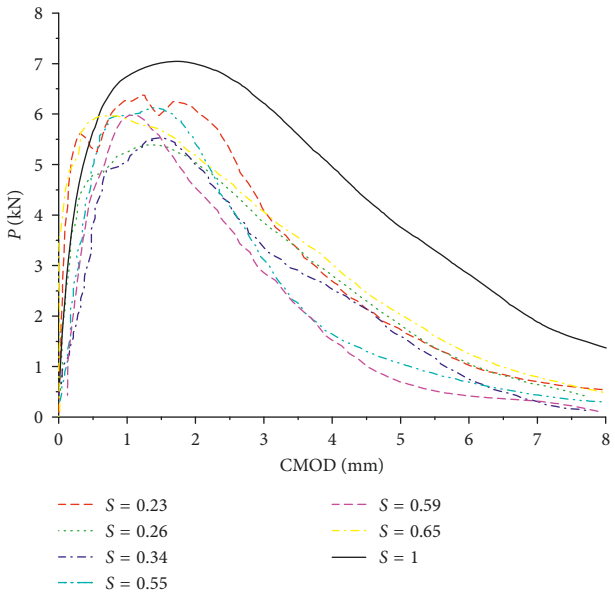

Figure 7: Evolution of CMOD curves after the dynamic test.

3.2. Dynamic Test Results. As shown in Table 3, specimens under different stress levels with the same number of cycles are tested in dynamic load. TPB is used as an abbreviation to the three-point bending specimen.

3.2.1. P-CMOD Curves. As shown in Figure 6, the maximum CMOD values of each fatigue cycle increase with the increment of the fatigue cycles. The CMOD values increase directly until the fatigue cycles reach approximately 1000, and the growth rate reduces under the stress levels of 0.55, 0.59, and 0.65. Nevertheless, the CMOD values increase directly under the stress levels of 0.23, 0.26, and 0.34 during the dynamic test.

Figure 7 shows the *P*-CMOD curves under static load after the fatigue cycles of 10,000. The difference of the ultimate load between the minimum stress level $S = 0.23$ and the maximum stress level $S = 0.65$ is just 0.42 kN, which is only 5.96% of the ultimate load under the static load. This illustrates that the ultimate load of specimens under 6 types of stress levels reduced smaller compared to the average load of failure specimens under the static load. Meanwhile, with the increment of

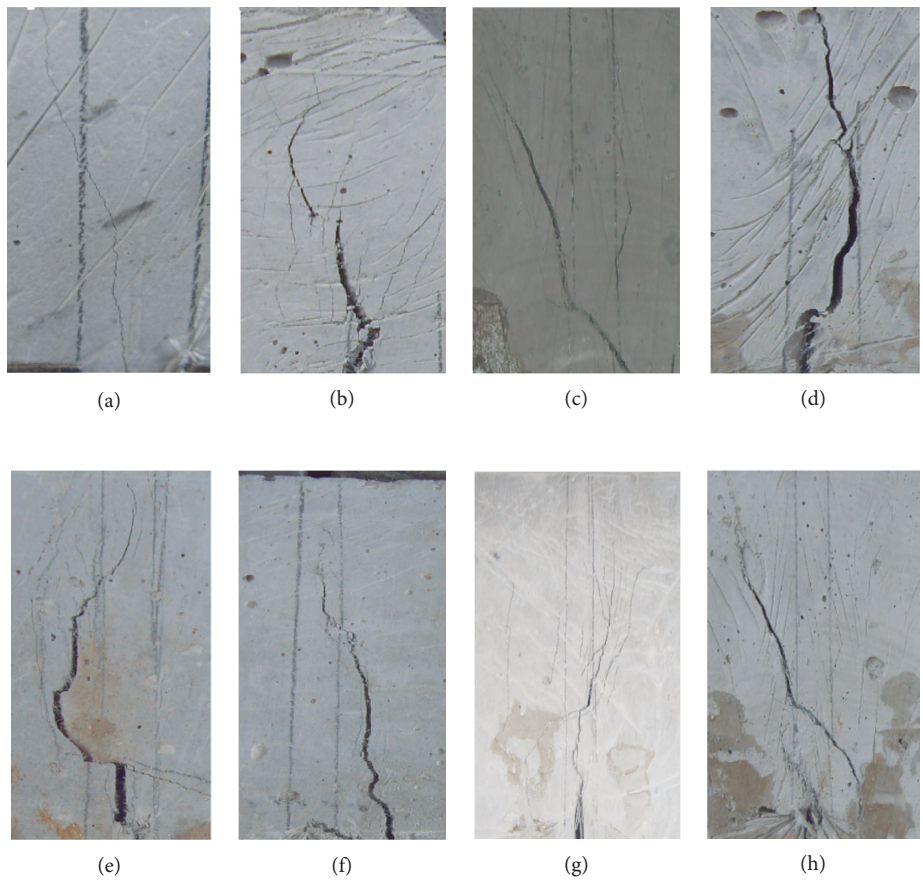

Figure 8: Side surfaces of ECC failure specimens under different stress levels. (a) Matrix. (b) $S = 1$. (c) $S = 0.655$. (d) $S = 0.59$. (e) $S = 0.55$. (f) $S = 0.34$. (g) $S = 0.26$. (h) $S = 0.23$.

Table 4: The test results during the dynamic test.

Stress level, S	1	0.65	0.59	0.55	0.34	0.26	0.23
Fatigue cycles	1	10,000	10,000	10,000	10,000	10,000	10,000
Number of cracks	27	17	13	11	7	6	4

stress levels, the strain-hardening capacity increased at first and then decreased. This demonstrates that more and more fibers participated in the fiber bridging during the dynamic test. Simultaneously, they were pulled out or broken in fatigue load with the decrease of the flexural capacity [10, 32, 33].

3.2.2. Cracking Mode and Transformation. As seen in Figure 8(a), the matrix specimen just has one tiny crack when it loses its bearing capacity. With adding PVA fibers into the matrix (Figure 8(b)), a large number of microcracks distribute around the initial crack edge in addition to the main crack, that is, multiple cracks under static load [31, 34, 35]. Figures 8(c)–8(h) illustrate the difference in cracking mode and length under different stress levels. The number of cracks of the specimens reduced with the decrease of the stress level. Meanwhile, the direction of propagation of the cracks was horizontal which reduced the stress concentration at the main crack edge [36]. Table 4 verified that the crack number reduces with the decreasing fatigue stress levels [14]. From the crack number and smooth degree in the either side of the main crack among Figures 8(b)–8(h), it can be observed that the specimens have the tendency of developing into brittle failure, still keeping the ductile failure.

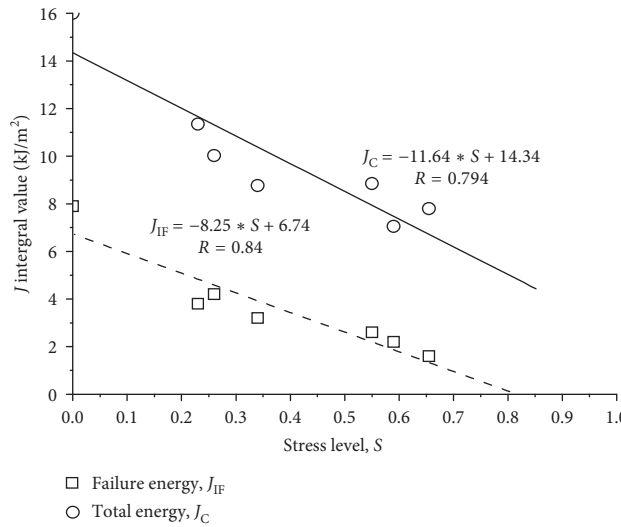

Figure 9: Relationship of the stress level and J integral.

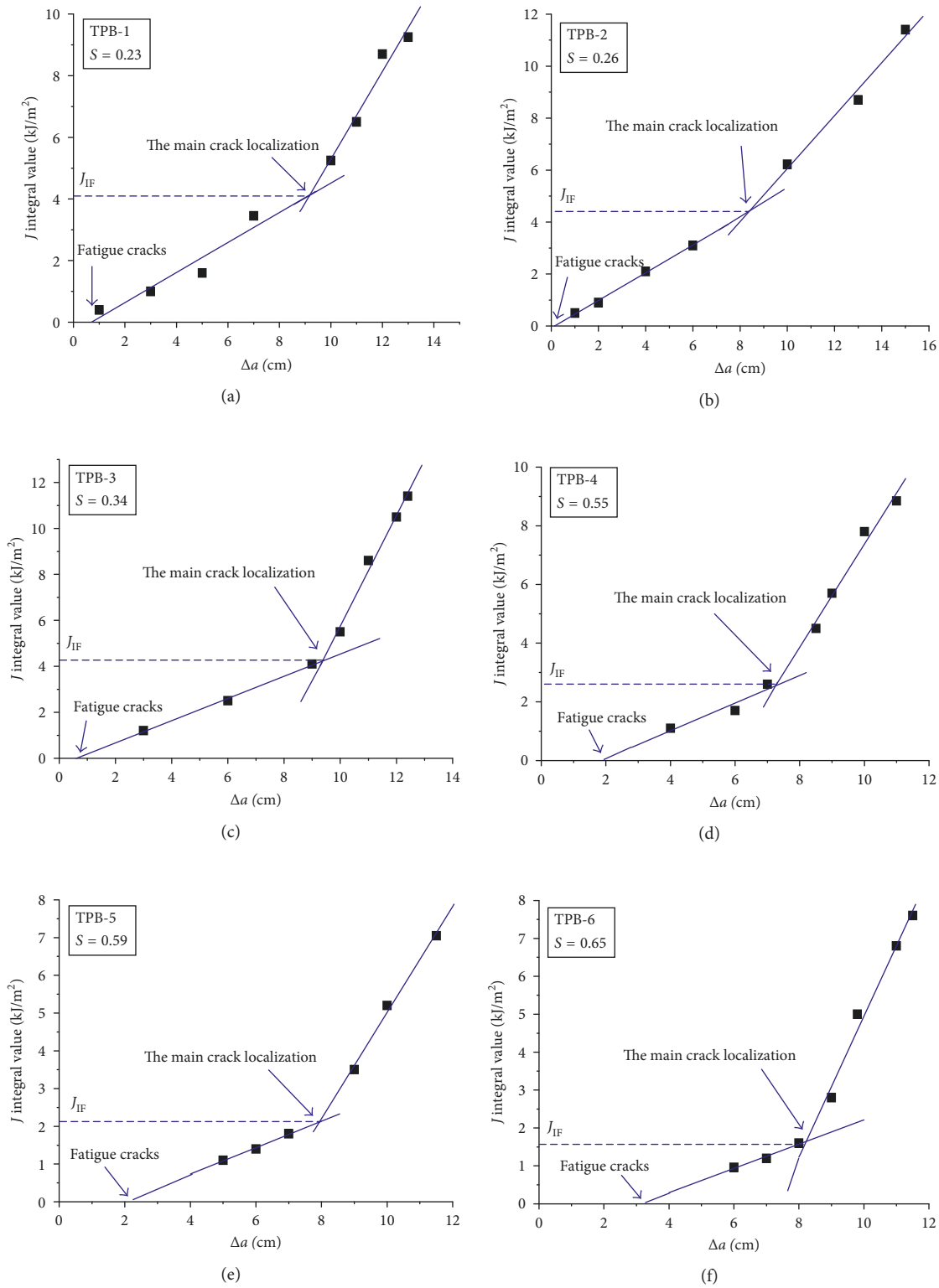

Figure 10: Relations between J integral and increment of the total crack length.

3.2.3. Fracture Toughness. The values of J_{IF} and J_C calculated by (5) with the experimental curves of P-CMOD are shown in Figure 9 [13]. From this diagram, it is clearly seen that the J_{IF}, the J integral value at the failure crack localizing point, and the total energy J_C decrease with the increase of stress levels. When $S = 0.817$ was calculated from the fitting formula, the J_{IF} value decreased to 0. This implies that the localized failure crack immediately developed under this stress level. The variation coefficients of 0.84 and 0.794 show that the formulas are still reliable. The contribution from this

formula might identify the ECC structures safe or not according to the stress levels.

3.2.4. J_R Resistance Curve. The J_R resistance curve stands for the relation between the crack extension and J integral value. During the test, it is observed that multicracks generate in the shapes of irregular curves. Hence, the single crack extension is not appropriate for ECC specimens. In this paper, the total crack length, a, is used to describe the crack extension of ECC specimens. During the experiment, the crack width observed is less than 60 μm before the main crack appears. This means that the ECC specimen starts to lose its bearing capacity when the crack width exceeds 60 μm. Therefore, the crack width can be neglected before the main crack appears, and only the total crack length is considered as the parameter.

The J integral values calculated by (5) with the experimental curves of P-CMOD are shown in Figure 7. Figure 10 shows the relationship between the increment of the total crack length Δa and the J integral values. Only one specimen is selected for each stress level. There were three linear relationships with two cutoff points of the crack development. In the first stage, very few cracks had been formed during the dynamic test, and the crack length Δa had appeared while J integral was kept zero. In the second stage, lots of cracks produced, and the crack length Δa increased with the increment of J integral values. In the third stage, the cracks developed quickly after localizing. J_{IF} can be calculated by (5) with P-CMOD curves shown in Figure 7. Moreover, the J_{IF} value can also be obtained by J-Δa curves. So, there are two methods to calculate the J_{IF} value. The results shown in Figure 11 illustrate that the two methods were almost equal. Therefore, the J_R curve can be applied to judge the fracture state of the ECC under low stress levels of fatigue.

Figure 10 illustrates the three linear relationships of the J_R resistance curve. In the second stage, J integral values increased with the increment of the crack length Δa. Equation (6) shows the relationship of J and Δa when the localized failure crack developed [13].

$$a = \Delta a + a' = \frac{J}{2\sigma_y} + a',$$
$$\Delta a = \frac{J}{2\overline{\sigma}_y} \left(0 < J < J_{IF}\right), \tag{6}$$

where a' represents the crack length generated in the dynamic test. $\overline{\sigma}_y$ is the residual equivalent yield stress. According to the J_R curves and (6), the results of $\overline{\sigma}_y$ obtained are shown in Figure 12. As seen, $\overline{\sigma}_y$ shows a decreasing trend, and the rates increase with higher stress levels [37].

4. Conclusion

This paper investigates the effect of low stress levels (0.23, 0.26, 0.34, 0.55, 0.59, and 0.65) on the mechanical and fracture properties of the ECC with 2% volume fraction of the PVA fiber. The following conclusions were drawn:

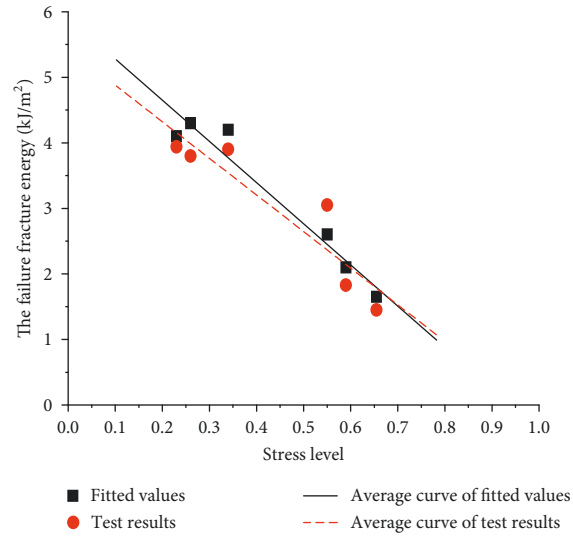

Figure 11: Comparison of J_{IF} results obtained from J_R resistance curves and experimental P-CMOD curves.

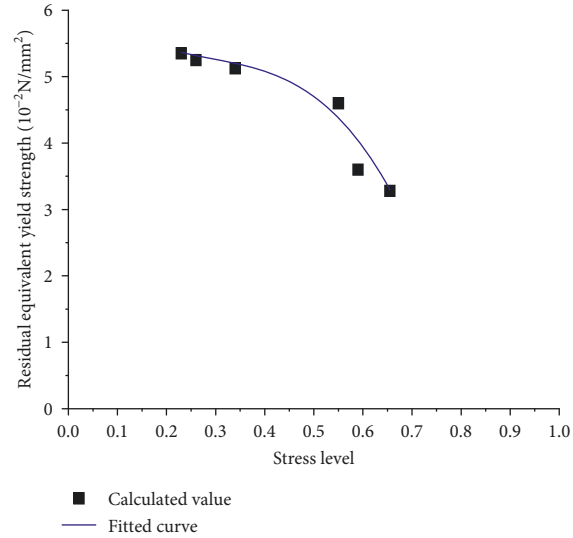

Figure 12: Calculated $\overline{\sigma}_y$ and fitted values from ECC's J_R curves.

(1) The fracture mode of the matrix was similar to that of the ECC. The difference between the initial cracking load and the ultimate load in the ECC was greater than that of the matrix. This shows that the fibers had the effect of bending resistance and of absorbing energy. The double J integral criterion testified the effect of fibers in the ECC.

(2) The capacity of strain hardening of the ECC increased at first and then decreased with the increment of stress levels. In contrast, the deformation ability of the ECC always decreased.

(3) The total crack length Δa was suitable to describe the fracture state of the ECC. The J_R curve of the ECC had three stages and two dividing points of fatigue cracking and crack localizing. Furthermore, the

linear relation of J integral and Δa in the stable stage indicated that the crack length developed regularly with the increase of fracture energy.

(4) The residual equivalent yield strength $\overline{\sigma}_y$ was applied to express the relationship between J integral and Δa in the second stage of J_R curves. The residual equivalent yield strength of the ECC decreased, and the rates increased with the increment of stress levels.

Conflicts of Interest

The authors declare that they have no conflicts of interest regarding the publication of this paper.

Acknowledgments

The authors gratefully acknowledge the financial supports provided by the National Natural Science Foundation of China (Project 51108151), the National Program on Key Basic Research Project (Project 2009CB623203), and the Natural Science Foundation of Hebei Province of China (Project E2012202097). This study was also part of a research project supported by China Three Gorges Corporation (Grant no. TGC-2012746379).

References

[1] M. Elices, G. V. Guinea, and J. Planas, "Measurement of the fracture energy using three-point bend tests: part 3—influence of cutting the P-δ tail," *Materials and Structures*, vol. 25, no. 6, pp. 327–334, 1992.

[2] V. C. Li and T. Hashida, "Engineering ductile fracture in brittle-matrix composites," *Journal of Materials Science Letters*, vol. 12, no. 12, pp. 898–901, 1993.

[3] J. Zhang, Z. Wang, X. Ju, and Z. Shi, "Simulation of flexural performance of layered ECC-concrete composite beam with fracture mechanics model," *Engineering Fracture Mechanics*, vol. 131, pp. 419–438, 2014.

[4] J. Zhang, C. K. Y. Leung, and Y. Gao, "Simulation of crack propagation of fiber reinforced cementitious composite under direct tension," *Engineering Fracture Mechanics*, vol. 78, no. 12, pp. 2439–2454, 2011.

[5] J. Zhang and H. Stang, "Interfacial degradation in cement-based fiber reinforced cement-based composites," *Journal of Materials Science Letters*, vol. 16, no. 11, pp. 886–888, 1997.

[6] J. Qiu and E. Yang, "Micromechanics-based investigation of fatigue deterioration of engineered cementitious composite (ECC)," *Cement and Concrete Research*, vol. 95, pp. 65–74, 2017.

[7] E. B. Pereira, G. Fischer, and J. A. O. Barros, "Effect of hybrid fiber reinforcement on the cracking process in fiber reinforced cementitious composites," *Cement and Concrete Composites*, vol. 34, no. 10, pp. 1114–1123, 2012.

[8] S. Müller and V. Mechtcherine, "Fatigue behaviour of strain-hardening cement-based composites (SHCC)," *Cement and Concrete Research*, vol. 92, pp. 75–83, 2017.

[9] S. G. Millard, T. C. K. Molyneaux, S. J. Barnett, and X. Gao, "Dynamic enhancement of blast-resistant ultra high performance fibre-reinforced concrete under flexural and shear loading," *International Journal of Impact Engineering*, vol. 37, no. 4, pp. 405–413, 2010.

[10] J. Zhang, H. Stang, and V. C. Li, "Fatigue life prediction of fiber reinforced concrete under flexural load," *International Journal of Fatigue*, vol. 21, no. 10, pp. 1033–1049, 1999.

[11] Z. Wu, S. Xu, J. Wang, and Y. Liu, "Double-k fracture parameter of concrete and its size effect by using three-point bending beam method," *Journal of Hydroelectric Engineering*, vol. 71, pp. 16–24, 2000.

[12] D. Y. Yoo, J. H. Lee, and Y. S. Yoon, "Effect of fiber content on mechanical and fracture properties of ultra high performance fiber reinforced cementitious composites," *Composite Structures*, vol. 106, pp. 742–753, 2013.

[13] W. Liu, S. Xu, and Q. Li, "Experimental study on fracture performance of ultra-high toughness cementitious composites with J-integral," *Engineering Fracture Mechanics*, vol. 96, pp. 656–666, 2012.

[14] E. H. Yang, S. Wang, and Y. Z. Yang, "Fiber-bridging constitutive law of engineered cementitious composites," *Journal of Advanced Concrete Technology*, vol. 6, no. 1, pp. 181–193, 2008.

[15] P. Kabele, "Multiscale framework for modeling of fracture in high performance fiber reinforced cementitious composites," *Engineering Fracture Mechanics*, vol. 74, no. 1-2, pp. 194–209, 2007.

[16] N. M. Altwair, M. A. Megat Johari, and S. F. Saiyid Hashim, "Flexural performance of green engineered cementitious composites containing high volume of palm oil fuel ash," *Construction and Building Materials*, vol. 37, pp. 518–525, 2012.

[17] Z. Lin and V. C. Li, "Crack bridging in fiber reinforced cementitious composites with slip-hardening interfaces," *Journal of the Mechanics and Physics of Solids*, vol. 45, no. 5, pp. 763–787, 1997.

[18] S. Xu and W. Liu, "Investigation on crack propagation law of ultra-high toughness cementitious composites under fatigue flexure," *Engineering Fracture Mechanics*, vol. 93, no. 1, pp. 1–12, 2012.

[19] V. C. Li, "Engineered cementitious composite (ECC): material, structural, and durability performance," in *Concrete Construction Engineering Handbook*, CRC Press, Boca Raton, FL, USA, 2007.

[20] S. H. Said, H. A. Razak, and I. Othman, "Flexural behavior of engineered cementitious composite (ECC) slabs with polyvinyl alcohol fibers," *Construction and Building Materials*, vol. 75, pp. 176–188, 2015.

[21] C. Lu, C. K. Y. Leung, and V. C. Li, "Numerical model on the stress field and multiple cracking behavior of engineered cementitious composites (ECC)," *Construction and Building Materials*, vol. 133, pp. 118–127, 2017.

[22] D. G. H. Latzko, *Post-Yield Fracture Mechanics*, Applied Science Publishers, London, UK, 1979.

[23] G. L. G. Gonzáles, J. A. O. González, J. T. P. Castro, and J. L. F. Freire, "A J-integral approach using digital image correlation for evaluating stress intensity factors in fatigue cracks with closure effects," *Theoretical and Applied Fracture Mechanics*, vol. 90, pp. 14–21, 2017.

[24] V. C. Li, *Engineered Cementitious Composites (ECC)–Tailored Composites through Micromechanical Modelling*, pp. 64–97, Canadian Society of Civil Engineers, Montreal, QC, Canada, 1998.

[25] M. Maalej, T. Hashida, and V. C. Li, "Effect of fiber volume fraction on the off-crack-plane fracture energy in strain-hardening engineered cementitious composites," *Journal of the American Ceramic Society*, vol. 78, no. 12, pp. 3369–3375, 2010.

[26] J. Li and Y. X. Zhang, "Evaluation of constitutive models of hybrid-fibre engineered cementitious composites under dynamic loadings," *Construction and Building Materials*, vol. 30, pp. 149–160, 2012.

[27] H. Li and S. Xu, "Determination of energy consumption in the fracture plane of ultra high toughness cementitious composite with direct tension test," *Engineering Fracture Mechanics*, vol. 78, no. 9, pp. 1895–1905, 2011.

[28] S. Xu and H. W. Reinhardt, "Determination of double-K criterion for crack propagation inquasi-brittle fracture, part III: compact tension specimens and wedge splitting specimens wedge splitting specimens," *International Journal of Fracture*, vol. 98, pp. 179–193, 1999.

[29] K. Duan, X. Z. Hu, and F. H. Wittmann, "Size effect on fracture resistance and fracture energy of concrete," *Materials and Structures*, vol. 36, no. 2, pp. 74–80, 2003.

[30] V. C. Li and H. C. Wu, "Conditions for pseudo strain-hardening in fiber reinforced brittle matrix composites," *Journal of Applied Mechanics Review*, vol. 45, no. 8, pp. 390–398, 1992.

[31] P. Jun and V. Mechtcherine, "Behaviour of strain-hardening cement-based composites (SHCC) under monotonic and cyclic tensile loading," *Cement and Concrete Composites*, vol. 32, no. 10, pp. 801–809, 2010.

[32] J. Zhang and V. C. Li, "Monotonic and fatigue performance in bending of fiber-reinforced engineered cementitious composite in overlay system," *Cement and Concrete Research*, vol. 32, no. 3, pp. 415–423, 2002.

[33] J. Zhang, H. Stang, and V. C. Li, "Experimental study on crack bridging in FRC under uniaxial fatigue tension," *Journal of Materials in Civil Engineering*, vol. 12, no. 1, pp. 65–73, 2000.

[34] S. He, J. Qiu, J. Li, and E. H. Yang, "Strain hardening ultra-high performance concrete (SHUHPC) incorporating CNF-coated polyethylene fibers," *Cement and Concrete Research*, vol. 98, pp. 50–60, 2017.

[35] W. Liu, S. Xu, and Q. Li, "Study on flexural fatigue life of ultra-high toughness cementitious composites under constant amplitude cyclic loading," *Journal of Building Structures*, vol. 33, pp. 119–127, 2012.

[36] Z. Zhang and S. Qian, "Investigating mechanical properties and self-healing behavior of micro-cracked ECC with different volume of fly ash," *Construction and Building Materials*, vol. 52, pp. 17–23, 2014.

[37] A. Skar, P. N. Poulsen, and J. F. Olesen, "A simple model for fatigue crack growth in concrete applied to a hinge beam model," *Engineering Fracture Mechanics*, vol. 181, pp. 38–51, 2017.